Materials Advances

ROYAL SOCIETY OF CHEMISTRY

PAPER

View Article Online
View Journal | View Issue

Cite this: *Mater. Adv.*, 2024, 5, 5624

A novel NIR fluorescent probe for *in situ* visualizing Fe(II) and its application in drug-induced liver/kidney injury†

Hanyue Xiang,[a] Yanjie Song,[a] Yilin Wang,[b] Wenzhuo Fu[c] and Nao Xiao *[a]

Fe^{2+} has high redox activity and participates in many important physiological processes *in vivo*, playing a crucial role in the living system. An excessive iron content can lead to oxidative stress and cell damage, leading to the occurrence of many diseases. Therefore, it is necessary to establish an effective method to detect unstable iron(II) ions (Fe^{2+}). In this work, a novel NIR fluorescent probe **MDJ-O** for Fe^{2+} based on the *N*-oxide structure was explored. The probe can monitor Fe^{2+} based on the ICT mechanism. In the PBS buffer solution containing 1 mM CTAB, **MDJ-O** showed a rapid response toward Fe^{2+} in 5 min with a fluorescence enhancement of 49-fold ($\lambda_{ex}/\lambda_{em}$ = 535/720 nm). The sensitivity of **MDJ-O** for Fe^{2+} was brilliant, and the detection limit was as low as 3.09 μM. Notably, **MDJ-O** was successfully utilized for living cell imaging and *in vivo* imaging of zebrafish and mice. In addition, **MDJ-O** was successfully used for monitoring the level changes of Fe^{2+} in the liver and kidney injuries induced by acetaminophen (APAP), achieving the visualization of the injury. This work is of great significance for the study of drug-induced liver and kidney injury and other iron-related diseases.

Received 5th April 2024,
Accepted 22nd May 2024

DOI: 10.1039/d4ma00361f

rsc.li/materials-advances

Introduction

Iron is the most plentiful transition metal element on Earth, and is utilized to maintain normal vital activities. Iron is closely related to human life and plays an important biological role. Labile iron with weak protein binding ability aggregates in the labile iron pool (LIP), exhibiting high redox activity.[1–6] In the microenvironment of cells, intracellular Fe^{3+} can be reduced to Fe^{2+} by ascorbic acid and reduced glutathione (GSH).[7,8] To maintain the ordinary function of cells in the organism, Fe^{2+} and Fe^{3+} need to be in equilibrium. Unstable Fe^{2+} can participate in the Fenton reaction to generate a hydroxyl radical (one of the reactive oxygen species (ROS)) which can cause serious oxidative damage to cells.[9–14] Iron deficiency can result in anemia, kidney damage, diabetes, *etc.*[15–18] On the other hand, excessive iron may lead to various diseases, such as Parkinson's disease, Alzheimer's disease, cardiovascular disease, cancer, *etc.*[19–21] Iron overload is also associated with liver and kidney injury.[22,23] For instance, acetaminophen (APAP), also known as paracetamol, is one of the most commonly used antipyretic and analgesic drugs. Excessive intake of APAP can induce severe liver and kidney toxicity, which can lead to acute liver failure (ALF) and acute kidney injury (AKI).[24,25] Although the molecular mechanism of liver and kidney toxicity induced by APAP is complicated, a few studies have revealed that the toxicity is associated with the increased Fe^{2+} level in the liver and kidney injury disease models.[26–29] Therefore, the establishment of an effective real-time detection method for biological Fe^{2+} ions is of great significance for further study of its physiological and pathological effects.

Up to now, some fluorescent probes have been developed as favorable tools for biosensing and imaging Fe^{2+} levels with significant advantages such as low cost, easy operation, and good selectivity.[30–36] However, the number of fluorescent probes used for detecting Fe^{2+} is still limited. There are mainly two kinds of Fe^{2+} fluorescent probes available, one is chelation-based probes and the other is reactivity-based probes (Scheme S1, ESI†).[37,38] Reaction-based Fe^{2+} fluorescent probes overcame some limitations of traditional chelating Fe^{2+} fluorescent probes, such as weak binding to Fe^{2+}, low selectivity, and poor *in vivo* imaging effect.[39,40] Due to the strong paramagnetic properties of iron ions, they have a strong fluorescence quenching ability. The "ON–OFF" response mode is susceptible to interference from complex biological systems and has poor sensitivity, which is not conducive to accurate

[a] *Beijing Area Major Laboratory of Peptide and Small Molecular Drugs, Engineering Research Center of Endogenous Prophylactic of Ministry of Education of China, School of Pharmaceutical Sciences, Capital Medical University, Beijing 100069, China. E-mail: xiaonao@ccmu.edu.cn*
[b] *School of Basic Medical Sciences, Capital Medical University, Beijing 100069, China*
[c] *Core Facilities Center, Capital Medical University, Beijing 100069, China*

† Electronic supplementary information (ESI) available. CCDC 2339716. For ESI and crystallographic data in CIF or other electronic format see DOI: https://doi.org/10.1039/d4ma00361f

identification and detection of Fe^{2+}. In contrast, a turn-on fluorescent probe can avoid the aforementioned limitations. In 2013, Nagasawa *et al.* developed the first fluorescent probe containing an *N*-oxide structure for Fe^{2+} with turn-on fluorescence in living cells.[41] *N*-oxide-based fluorescent probes can quickly capture the changes in the Fe^{2+} level in both *in vivo* and *in vitro*, which has greatly attracted the attention of many researchers. In the past decade, some researchers have introduced the *N*-oxide structure as the recognition site for Fe^{2+} into different kinds of fluorophores and applied them to the detection of Fe^{2+} (Table S4, ESI†). Near-infrared (NIR) fluorescent probes have been applied in the field of bioanalysis, owing to the great advantages of a good tissue penetration depth and non-invasive detection *in vivo*.[42,43] Therefore, the development of novel fluorescent probes toward Fe^{2+} with good water solubility, high selectivity, rapid response, and near-infrared fluorescence characteristics has been a research hotspot.

Here, we developed a novel NIR fluorescent probe **MDJ-O** containing an N-oxide structure on the julolidine moiety. The probe emitted NIR fluorescence when reacting with Fe^{2+}. **MDJ-O** could effectively detect Fe^{2+} in nearly 100% aqueous solution, living cells, zebrafish, and mice. After Fe^{2+} mediated deoxidation of the *N*-oxide structure, intramolecular charge transfer (ICT) was enhanced, and about 49-fold increase of the NIR fluorescence emission (λ_{em} = 720 nm) was observed. The probe displayed brilliant selectivity and sensitivity toward Fe^{2+}, and could achieve a specific fluorescence turn-on response towards Fe^{2+} within 5 min. Imaging experiments showed that **MDJ-O** had low cytotoxicity and good biocompatibility, and could be used to image endogenous and exogenous Fe^{2+} in cells, zebrafish, and mice. In addition, probe **MDJ-O** was successfully utilized to visualize Fe^{2+} in mice with APAP-induced liver and kidney injury. This is of great significance for further exploring the occurrence and development process of liver and kidney injury.

Experimental section

Synthesis and characterization

Synthesis of 2-(3,5,5-trimethylcyclohex-2-en-1-ylidene) malononitrile (1). Isophorone (1.26 g, 19.08 mmol) and malononitrile (2.77 g, 20.10 mmol) were dissolved in 10 mL of absolute EtOH, and then piperidine (269.74 mg, 3.17 mmol) and acetic acid (190.26 mg, 3.17 mmol) were slowly added to it, respectively. The reaction solution was stirred at 60 °C for 12 h and monitored by TLC. After the raw material isophorone was completely consumed, the reaction was stopped. The solvent was evaporated under reduced pressure. The crude product was purified by silica gel column chromatography using dichloromethane (CH_2Cl_2) to afford **1** as yellow solid powder. Yield: 2.80 g (78.87%). ^{1}H NMR (DMSO-d_6 300 MHz): δ (ppm) 6.60 (s, 1H), 2.27 (s, 2H), 2.09 (s, 3H), 1.00 (s, 6H) (Fig. S1, ESI†). ^{13}C NMR (DMSO-d_6 75 MHz): δ (ppm) 171.24, 162.27, 119.38, 113.34, 112.56, 76.09, 44.74, 41.89, 31.90, 27.21 (Fig. S2, ESI†). ESI-MS (*m*/*z*): 185.68 $[\mathbf{1}–H^+]^-$ (cacld for $C_{12}H_{13}N_2^-$: 185.11) (Fig. S3, ESI†).

Synthesis of MDJ. **1** (558.36 mg, 3.0 mmol) and 2,3,6,7-tetrahydro-1*H*,5*H*-benzo[*ij*]quinolizine-9-carboxaldehyde (603.35 mg, 3.1 mmol) were dissolved in 10 mL of absolute EtOH, and then excessive dimethylamine methanol solution was slowly added to it. The reaction solution was stirred under reflux for 8 h and monitored by TLC. After the raw material **1** was completely consumed, the reaction was stopped. The resultant black-blue powder was filtered and subsequently washed thrice with cold EtOH solution to remove unreacted raw materials. Yield: 0.98 g (83.76%). ^{1}H NMR ($CDCl_3$ 300 MHz): δ (ppm) 6.85 (m, 5H), 3.26 (t, J = 5.25 Hz, 4H), 2.75 (t, J = 5.91 Hz, 4H), 2.55 (s, 2H), 2.42 (s, 2H), 1.97 (m, 4H), 1.05 (s, 6H). ^{13}C NMR ($CDCl_3$ 75 MHz): δ (ppm) 169.14, 155.75, 144.92, 138.89, 127.45, 123.47, 122.81, 121.45, 120.95, 114.68, 113.87, 74.82, 50.15, 43.16, 39.42, 32.11, 28.20, 27.84, 21.70. ESI-MS (*m*/*z*): 370.19 [**MDJ** + H^+]$^+$ (cacld for $C_{25}H_{28}N_3^+$: 370.23).

Synthesis of MDJ-O. **MDJ** (812 mg, 2.2 mmol) was dissolved in 10 mL of EtOAc, and then ***m*-CPBA** (603.35 mg, 3.1 mmol) was slowly added to the reaction solution at 0 °C. The reaction solution was stirred at room temperature for 5 h and monitored by TLC. After the raw material **MDJ** was completely consumed, the reaction was stopped. The reaction solution was filtered to obtain a pale yellow product. Then the powder was washed thrice with EtOAc to remove unreacted raw materials. Yield: 0.91 g (71.09%). ^{1}H NMR ($CDCl_3$ 300 MHz): δ (ppm) 7.18 (s, 2H), 6.88 (m, 3H), 4.67 (d, J = 11.73 Hz, 2H), 3.56 (td, J = 12.48, 3.45 Hz, 2H) 3.16 (m, 4H), 2.97 (m, 2H), 2.61 (s, 2H), 2.43 (s, 2H), 2.09 (m, 2H), 1.08 (s, 6H). ^{13}C NMR ($CDCl_3$ 75 MHz): δ (ppm) 169.34, 152.91, 136.89, 134.46, 131.62, 129.79, 128.17, 127.16, 124.72, 113.37, 112.35, 80.11, 65.30, 43.20, 39.34, 32.04, 28.19, 25.35, 16.43. ESI-MS (*m*/*z*) 386.30 [**MDJ-O** + H^+]$^+$ (cacld for $C_{25}H_{28}N_3O^+$: 386.22).

All experiments were performed in compliance with the relevant laws and institutional guidelines, and were approved by the ethical committee at Capital Medical University.

Results and discussion

Design and synthesis of probe MDJ-O

In this work, a novel NIR Fe^{2+} fluorescent probe **MDJ-O** based on the julolidine moiety was designed and synthesized. The probe was easily synthesized in only two steps, and the pure products **MDJ** and **MDJ-O** were obtained by just washing without purification by column chromatography. **MDJ** was synthesized by the Knoevenagel condensation reaction of **1** and 2,3,6,7-tetrahydro-1*H*,5*H*-benzo[*ij*]quinolizine-9-carboxaldehyde (Scheme 1A). The hyperoxide reagent ***m*-CPBA** was used to oxidize the tertiary amine of **MDJ** to the *N*-oxide structure on **MDJ-O** (Scheme 1B). According to the literature, **MDJ-O** is the first NIR fluorescent probe toward Fe^{2+} based on the structure of julolidine. The structures of **MDJ** and **MDJ-O** were characterized by ^{1}H NMR, ^{13}C NMR, and ESI-MS (Fig. S4–S10, ESI†). The structure of **MDJ** ($C_{25}H_{27}N_3$) was further confirmed by X-ray single-crystal analysis (Fig. S7, ESI†). All the important

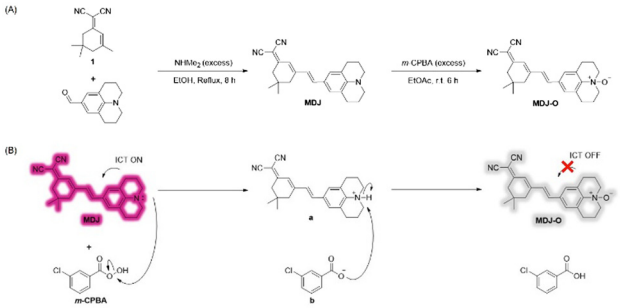

Scheme 1 (A) Synthetic route of probe **MDJ-O**. (B) Proposed synthesis mechanism of probe **MDJ-O** using ***m*-CPBA**.

crystallographic data (CCDC 2339716†) and refinement parameters are given in Tables S1–S3 (ESI†). **MDJ** was a monoclinic crystal system, and it could be known from Table S1 and Fig. S7 (ESI†). In fact, the single bond in the **MDJ** structure could rotate to produce two isomers, **MDJ** and **MDJ′** (Fig. S7, ESI†). According to the X-ray crystal structure of **MDJ**, it should exist in the **MDJ** structure rather than the **MDJ′** structure.

Spectral response of probe MDJ-O towards Fe^{2+}

To understand the fluorescence response of **MDJ-O** toward Fe^{2+} in different solvents, Fe^{2+} was added to different solvents containing **MDJ-O**. As shown in figures (Fig. S12 and S13, ESI†), the fluorescence intensities of **MDJ-O** towards Fe^{2+} in organic solution were generally higher than that in aqueous solution. This may be due to the fact that **MDJ-O** was more soluble in the organic phase. It was worth noting that the fluorescence intensity of the solution was obviously increased after adding CTAB to the PBS buffer solution. CTAB as a cationic surfactant is composed of a hydrophilic quaternary ammonium salt and a hydrophobic non-polar hydrocarbon chain. CTAB could form stable micelles by self-assembly in water.[44–46] The enhanced fluorescence intensity of an aqueous solution containing CTAB might contribute to the formation of micelles. CTAB encapsulated **MDJ-O** into hydrophobic cavities to form micelles (Scheme 2), which increased the solubility of **MDJ-O** in aqueous systems and promoted its response to Fe^{2+} in an aqueous environment (Fig. S14, ESI†). As shown in Fig. S15 (ESI†), the fluorescence intensities increased with the increase in CTAB concentration, indicating that the fluorescence intensity was concentration-dependent on CTAB. A hypothesis had been proposed that the increase of CTAB concentration expanded the size of the hydrophobic cavity, weakened the collision between fluorescent particles, reduced the non-radiative transition of molecules, increased the fluorescence efficiency, and thus increased the fluorescence intensity. In addition, as the concentration of CTAB increased, more probe molecules could be encapsulated in the micelles. This process promoted the solubility of the probes in aqueous solution, resulting in a high reaction probability of **MDJ-O** towards Fe^{2+} and fluorescence enhancement. To understand the properties of the micelles, the particle size of the micelles in PBS buffer was measured using the dynamic light scattering (DLS) method. DLS test results

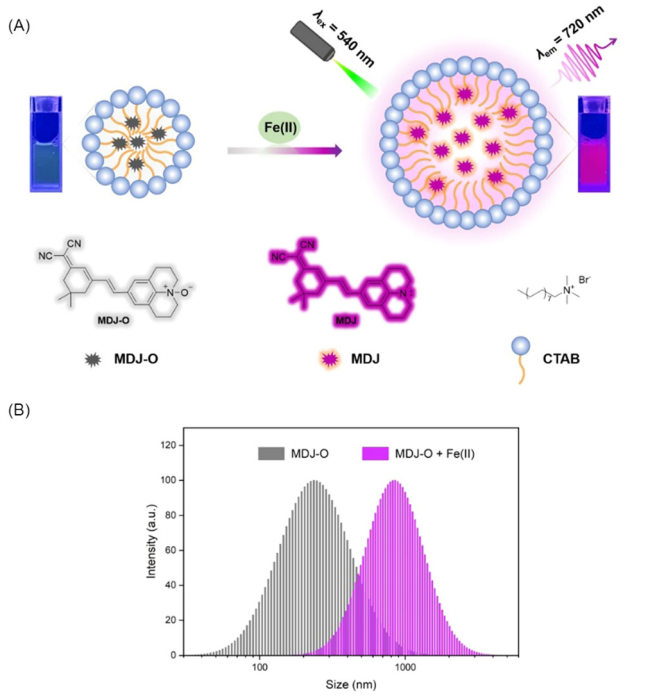

Scheme 2 (A) Response mechanism of **MDJ-O** towards labile Fe^{2+} in PBS buffer solution. (B) The size distribution of **MDJ-O** (10 μM) dispersed in PBS buffer solution with or without adding Fe^{2+} (100 μM).

showed that the particle size of the **MDJ-O** was about 200 nm, and the particle size was expanded to about 900 nm after adding Fe^{2+} to the **MDJ-O** solution (Fig. S16, ESI†). This may be due to the reaction of **MDJ-O** with Fe^{2+} to yield **MDJ**. The molecule **MDJ** is more hydrophobic than **MDJ-O**, and it could be easily wrapped in the hydrophobic cavity. As the number of molecules entering the hydrophobic cavity increased, the micelle size also increased.

As shown in the UV-vis absorption spectrum (Fig. 1A), the maximum absorption peak of **MDJ-O** (10 μM) at 390 nm in PBS buffer solution. After the addition of Fe^{2+} (100 μM), the maximum absorption peak was redshifted to 550 nm, and the color of the solution changed from light yellow to purple. In addition, the fluorescence excitation and emission spectra of **MDJ** and **MDJ-O** + Fe^{2+} were recorded (Fig. S17, ESI†). The excitation wavelengths of **MDJ** and **MDJ-O** + Fe^{2+} were similar, and the emission wavelengths were the same, indicating that **MDJ-O** reacted with Fe^{2+} to generate **MDJ**. Upon excitation at 540 nm, **MDJ-O** did not emit fluorescence. After treatment with Fe^{2+} (100 μM), the fluorescence intensity significantly increased at 720 nm (Fig. S18, ESI†). The above results indicated that Fe^{2+} mediated the deoxidation of **MDJ-O**, releasing the fluorophore **MDJ** and exhibiting an "OFF–ON" fluorescence response, and proved that **MDJ-O** could effectively detect Fe^{2+}.

To further study the stability of **MDJ-O** and **MDJ-O** towards Fe^{2+}, the fluorescence intensities of both systems were monitored in real-time for 2 h. The dynamic analysis results indicated that the probe **MDJ-O** solution had a low and stable fluorescence intensity at 720 nm. When Fe^{2+} (100 μM) was

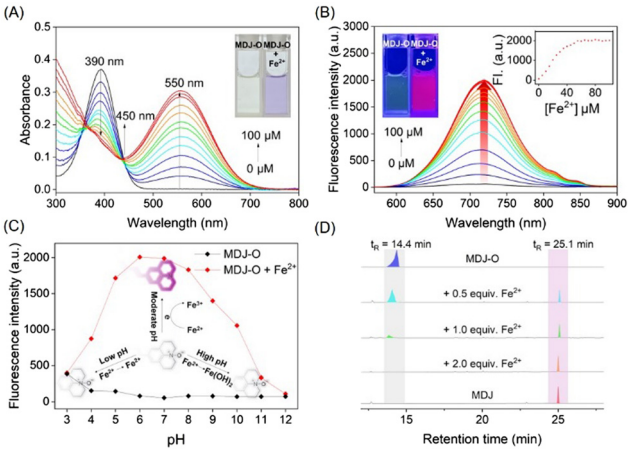

Fig. 1 (A) The UV-vis spectra of probe **MDJ-O** (10 μM) in response to increasing concentrations of Fe^{2+} (0–100 μM) in PBS buffer. (B) Fluorescence emission spectra of probe **MDJ-O** (10 μM) in response to increasing concentrations of Fe^{2+} (0–100 μM) in PBS buffer. (C) Fluorescence emission intensities (720 nm) of probe **MDJ-O** (10 μM) at varied pH values in the absence/presence of Fe^{2+} (100 μM). (D) HPLC of **MDJ-O**, **MDJ-O** with Fe^{2+}, and **MDJ**.

added to the **MDJ-O** solution, the fluorescence intensity of the solution increased rapidly. It reached a plateau in 5 min, completing the recognition of Fe^{2+} and enhancing the fluorescence intensity 49-fold (Fig. S19, ESI†). **MDJ-O** had a rapid response to Fe^{2+}, which was faster than most of the reported *N*-oxide-based probes. This feature illustrated that **MDJ-O** had obvious advantages in the detection of Fe^{2+}.

To investigate the response-ability of probe **MDJ-O** to Fe^{2+}, UV-vis titration and fluorescence titration experiments were carried out. As shown in Fig. 1A, new absorption peaks at 550 nm increased significantly after the continuous addition of Fe^{2+} (0–100 μM) to PBS buffer solution containing probe **MDJ-O** (10 μM). The absorption peaks at 390 nm gradually decreased upon increasing the concentration of Fe^{2+} ions, and a distinct isosbestic point appeared at 430 nm. This indicated that **MDJ-O** reacted with Fe^{2+} to form the new substance **MDJ**. The new absorption peak of **MDJ-O** + Fe^{2+} at 550 nm was consistent with the absorption wavelength of **MDJ**, which further indicated that **MDJ-O** reacted with Fe^{2+} to form **MDJ**. As shown in Fig. 1B, with the increase of Fe^{2+} concentration (0–100 μM), the fluorescence intensity at 720 nm gradually increased. The observed color of the solution changed from light yellow to bright purple by irradiation with an ultraviolet lamp (λ_{ex} = 365 nm). The fluorescence intensity of probe **MDJ-O** (10 μM) at 720 nm displayed a good linear relationship with the concentration of Fe^{2+} (0–35 μM) (Fig. S20, ESI†). The limit of detection (LOD) of **MDJ-O** for Fe^{2+} was calculated to be 3.06 μM. From the above results, it could be concluded that probe **MDJ-O** had high sensitivity to Fe^{2+} and could meet the detection requirements for Fe^{2+} in biological systems and environmental samples.

pH response of MDJ-O towards Fe^{2+}

To investigate the applicability of probe **MDJ-O** *in vivo*, a pH-dependent assay of the probe was performed. The fluorescence emission intensities of **MDJ-O** and **MDJ-O** towards Fe^{2+} were performed in PBS buffer solution. As shown in Fig. 1C, the fluorescence of **MDJ-O** at 720 nm did not change obviously with the change of pH value, indicating that probe **MDJ-O** had good stability and was unaffected by the change of pH (3–12). After adding Fe^{2+} (100 μM) to probe **MDJ-O** (10 μM), the probe showed a significant fluorescence enhancement response in the pH range 4–9 (Fig. 1C). Under the conditions of strong acid and strong base, the fluorescence enhancement amplitude was small, and even tended to the fluorescence intensity of **MDJ-O**. This may be because Fe^{2+} was relatively stable and not easily converted to Fe^{3+} under strongly acidic conditions, which leads to the Fe^{2+} being unable to provide electrons and hard to react with **MDJ-O** to release **MDJ**. In the presence of a strong base, Fe^{2+} was more likely to react with OH^- to form an $Fe(OH)_2$ precipitate, which reduced the reaction chance of **MDJ-O** with Fe^{2+}, making redox reactions hard to occur, resulting in a poor fluorescence response. In summary, **MDJ-O** revealed a significant fluorescence response towards Fe^{2+} within the physiological pH range, which was suitable for the detection of Fe^{2+} in complex physiological environments.

Selective testing of MDJ-O for Fe^{2+}

To explore the specific detection ability of probe **MDJ-O** towards Fe^{2+}, different cations, anions, amino acids, and bioactive analytes were used to evaluate the selectivity of probe **MDJ-O**. After adding the analytes, only the absorption peaks of **MDJ-O** can be observed in the UV-vis absorption spectra. After Fe^{2+} was added to the solution containing **MDJ-O**, a new absorption peak appeared at 550 nm (Fig. 2A). In the bright field, the color of the sample solution changed from light yellow to purple, which could be easily identified by the naked eye, indicating that the probe molecule can directly detect Fe^{2+} by the colorimetric method. According to the fluorescence spectra, no obvious fluorescence response at 720 nm was observed after mixing the probe with other analytes. In striking contrast, a significant fluorescence enhancement was detected with the solution containing **MDJ-O** (10 μM) and Fe^{2+} (100 μM) (Fig. S21, ESI†). As shown in the inset of Fig. 2B, only the probe solution towards Fe^{2+} emitted strong fluorescence under the excitation

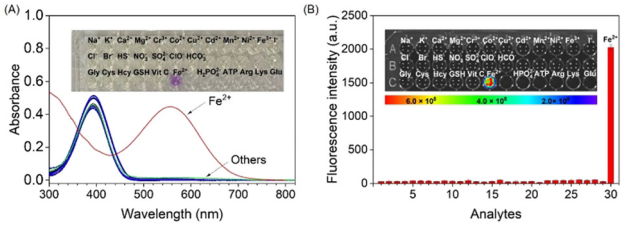

Fig. 2 (A) UV-vis spectral changes of **MDJ-O** (10 μM) with the addition of 10 equivalents of various analytes. Inset: Bright field photograph of the probe **MDJ-O** solution (10 μM) upon addition of 10 equivalents of various analytes. (B) The bar graph comparison of the fluorescence intensities of **MDJ-O** (10 μM) towards various analytes (100 μM). Inset: The photograph of free **MDJ-O** and **MDJ-O** upon adding various analytes under 561 nm light irradiation.

light of 540 nm. The experimental results showed that the probe had brilliant selectivity and could only detect Fe^{2+}, but not other analytes.

To further demonstrate the high specificity of probe **MDJ-O** towards Fe^{2+}, competitive experiments were conducted to investigate the anti-interference ability of **MDJ-O** in PBS buffer solution. The addition of 100 μM interfering analytes to the solution containing the probe alone did not induce an obvious fluorescence change. After adding Fe^{2+} (100 μM) to the aforementioned solutions, the fluorescence intensities increased significantly (Fig. S22, ESI†). Among them, the fluorescence enhancement effect was disturbed by Cu^{2+}, which may be attributed to the paramagnetism of Cu^{2+}. To sum up, the detection of Fe^{2+} by probe **MDJ-O** was free from the interference of most analytes, showing high selectivity and strong anti-interference ability in aqueous solution.

Response mechanism of MDJ-O to Fe^{2+}

The response mechanism of **MDJ-O** to Fe^{2+} was preliminarily explained by the experiments of UV-vis titration and fluorescence titration. To further verify the response mechanism of **MDJ-O** towards Fe^{2+}, ESI-MS and HPLC were used to further explore the response mechanism. After mixing **MDJ-O** with Fe^{2+} in the methanol solution, the peak of **MDJ-O** at 386.22 *m*/*z* and the peak of the deoxidation product **MDJ** at 370.19 *m*/*z* were detected in the mass spectrum (Fig. S11, ESI†). This result indicated that in the presence of Fe^{2+}, **MDJ-O** was deoxidized to form the parent fluorophore **MDJ**. As shown in the HPLC results (Fig. 1D), the retention time of **MDJ-O** was 14.4 min and that of **MDJ** was 25.1 min. After the reaction of **MDJ-O** with 0.5, 1, 2, and 5 equivalents of Fe^{2+}, the peak intensities at 14.4 min gradually decreased with the increase of the Fe^{2+} content, and the peak intensities at 25.1 min gradually increased. When 2 equivalents of Fe^{2+} were added to the solution containing **MDJ**, only the peak of **MDJ** was visible. These results further elucidated that the **MDJ-O** could be converted to **MDJ** by reacting with Fe^{2+}.

To further confirm the theoretical mechanism of the **MDJ-O** response to Fe^{2+}, DFT calculations were performed using the Gaussian 16 program.[47,48] Geometry optimization was completed at the B3LYP-D3BJ/TZVP level, in combination with the SMD implicit solvation model to take account of the solvation effect of DMSO. Fig. 3 shows the electrostatic potential mapped molecular surfaces of **MDJ-O**/**MDJ**. The lowest occupied molecular orbital (LUMO) of **MDJ-O** is mainly distributed on the dinitrilyl isophorone moiety, and the highest occupied molecular orbital (HOMO) is distributed on the N–O site of the julolidine moiety. It is clearly shown that the distribution of the HOMO and LUMO on **MDJ-O** exhibits significant spatial separation, leading to a potential PET quenching pathway of its fluorescence. After **MDJ-O** reacted with Fe^{2+}, **MDJ** was released and the HOMO was transferred to the whole skeleton of the fluorophore. The PET process was inhibited, resulting in enhanced fluorescence. The ΔE values of **MDJ-O** and **MDJ** were 2.73 eV and 2.33 eV, respectively. The energy gap of **MDJ** is smaller than that of **MDJ-O**, which is consistent with the redshift phenomenon of the emission and absorption wavelengths of **MDJ** compared with that of **MDJ-O**.

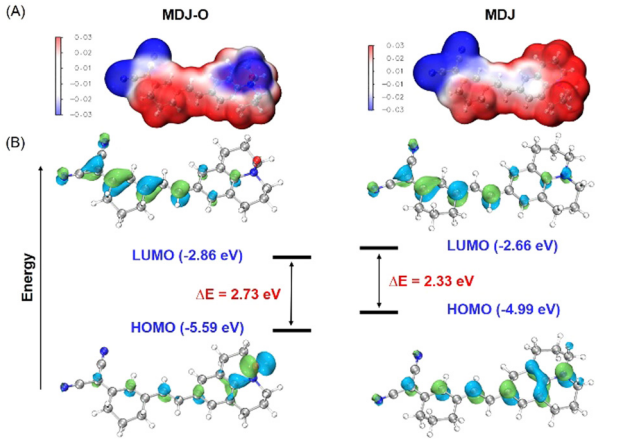

Fig. 3 (A) The molecular surface electrostatic potentials of **MDJ-O** and **MDJ** were depicted using the VMD program. (B) Frontier orbitals and orbital energies of the structures of **MDJ-O** and **MDJ**.

Imaging of Fe^{2+} in living cells

Based on the excellent optical properties of **MDJ-O** in aqueous solution, the potential application of **MDJ-O** for the detection of Fe^{2+} in living cells was explored. The cytotoxicity of the probe in HepG2 cells was first evaluated by the MTT assay prior to the cell imaging experiments. As shown in Fig. S23 (ESI†), more than 90% of survival rates were found after the HepG2 cells were treated with **MDJ-O** (10–30 μM) for 24 h. This result suggested that **MDJ-O** exhibited low cytotoxicity to HepG2 cells and could be further applied to monitor Fe^{2+} in living HepG2 cells. Subsequently, the detection of Fe^{2+} with **MDJ-O** in living cells was performed by laser confocal microscopy. As shown in Fig. 4B, only a weak fluorescence signal was observed after the cells were treated with **MDJ-O** (10 μM) for 30 min. In the **MDJ-O** + Fe^{2+} group, significant fluorescence could be monitored after the cells were loaded with **MDJ-O** (10 μM) and Fe^{2+} (100 μM) in sequence. The result apparently showed that **MDJ-O** can utilize fluorescence imaging to demonstrate exogenous Fe^{2+} levels of cells. To further verify that the fluorescence enhancement was mediated by Fe^{2+}, the Fe^{2+} chelating agent 2,2′-bipyridine (Bpy) was used to chelate Fe^{2+} in cells. After the cells were treated with Bpy (1 mM), the cells containing only **MDJ-O** showed weak fluorescence. When the cells containing **MDJ-O** and Fe^{2+} were pretreated with Bpy (1 mM), the fluorescence intensity in cells was significantly decreased (Fig. S24, ESI†). These experimental studies further confirmed that **MDJ-O** could detect both endogenous and exogenous Fe^{2+} in living cells by turn-on fluorescence. To study the stability of **MDJ-O** in living cells, photostability experiments were carried out. Red fluorescence was released after the recognition of Fe^{2+} by **MDJ-O**, and the fluorescence signal did not fade significantly within 1 h. The results showed that **MDJ-O** had good stability and strong anti-quenching ability in living cells (Fig. S25, ESI†). In addition, the subcellular localization of the obtained fluorescence was

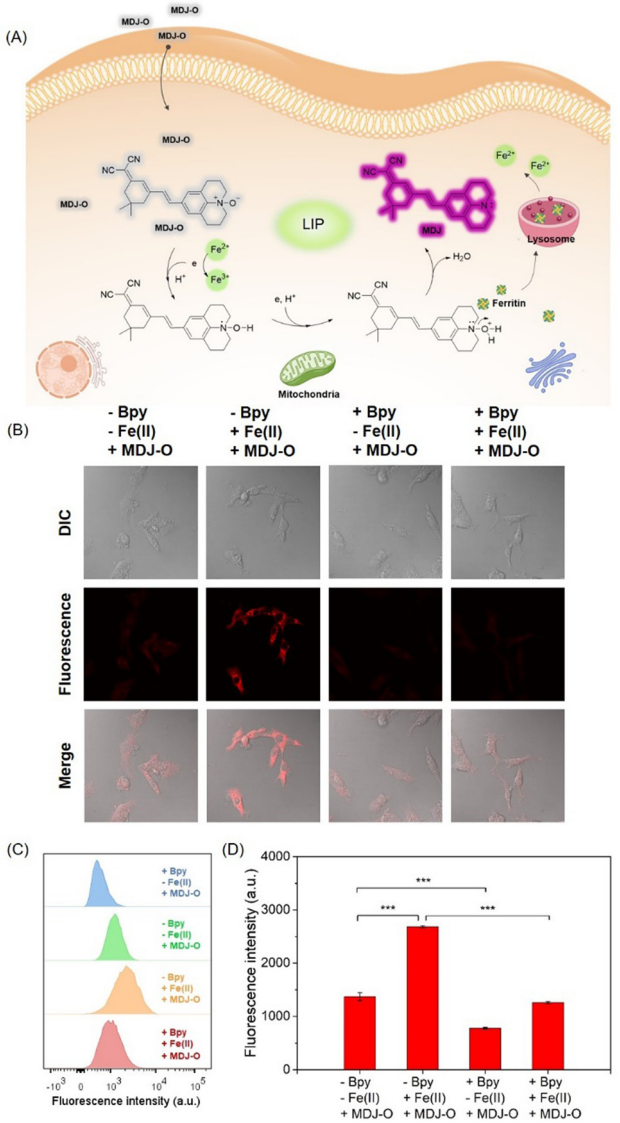

Fig. 4 (A) Proposed mechanism of probe **MDJ-O** towards Fe^{2+} in living cells. (B) Confocal imaging of Fe^{2+} in HepG2 cells by using probe **MDJ-O** (10 μM). (C) Flow cytometry histogram results. (D) Mean observed fluorescence intensities of *C* by flow cytometry. Statistical analysis was performed with a Student's *t*-test. $^{**}P < 0.01$ and $^{***}P < 0.001$ ($n = 3$). Error bars indicate ± S.E.M.

investigated. The fluorescence generated by **MDJ-O** upon treatment with Fe^{2+} had poor overlap with mitochondrial dyes (Fig. S26, ESI†), and the Pearson correlation coefficient was 0.55. To our delight, there was good overlap between the fluorescence generated by "**MDJ-O** + Fe^{2+}" and LysoTracker (Fig. S27, ESI†), the Pearson correlation coefficient was 0.87. This phenomenon indicated that a higher level of Fe^{2+} exists in lysosomes and probe **MDJ-O** can effectively monitor it.

Detection of intracellular Fe^{2+} by flow cytometry

In order to quantitatively analyze the intracellular fluorescence intensity, flow cytometry analysis experiments were conducted. As shown in Fig. 4C, the flow cytometry results of the four groups of cells are represented by a green peak surface, orange peak surface, blue peak surface, and red peak surface, respectively. Among them, the intracellular fluorescence signal of the **MDJ-O** + Fe^{2+} group was higher than that of the other groups. After being treated with Bpy (1 mM, 1 h), the fluorescence signal of the **MDJ-O** + Fe^{2+} group shifted from the high signal region to the low signal region, indicating that Bpy could chelate exogenous Fe^{2+}. These results also reflect that probe **MDJ-O** can detect exogenous Fe^{2+} ions in cells. The fluorescence signal in the Bpy + **MDJ-O** group was lower than that in the **MDJ-O** group, indicating that probe **MDJ-O** could monitor endogenous Fe^{2+}. The above results demonstrated that **MDJ-O** can detect endogenous and exogenous Fe^{2+} ions in cells by brilliant sensitivity (Fig. 4C and D).

In vivo and tissue imaging

Based on the excellent imaging performance of probe **MDJ-O** in HepG2 cells, the potential ability of probe **MDJ-O** to image Fe^{2+} *in vivo* was further explored. Adult zebrafish was selected as one of the animal models in this study, this is mainly due to the high proportion of homologous genes between zebrafish and humans.[49,50] As illustrated in Fig. 5A, there was no fluorescence in the control group, while weak fluorescence could be observed when zebrafish were cultured with **MDJ-O** (10 μM) alone. This phenomenon indicated that **MDJ-O** processes the turn-on fluorescence response to endogenous Fe^{2+} in zebrafish. After the zebrafish were cultured with Fe^{2+} (100 μM) for 30 min and then treated with **MDJ-O** (10 μM) for another 30 min, strong fluorescence in the gill and abdomen of zebrafish could be observed. Moreover, with an increase of the Fe^{2+} concentration (0, 10, 20, and 50 μM), the fluorescence intensities in

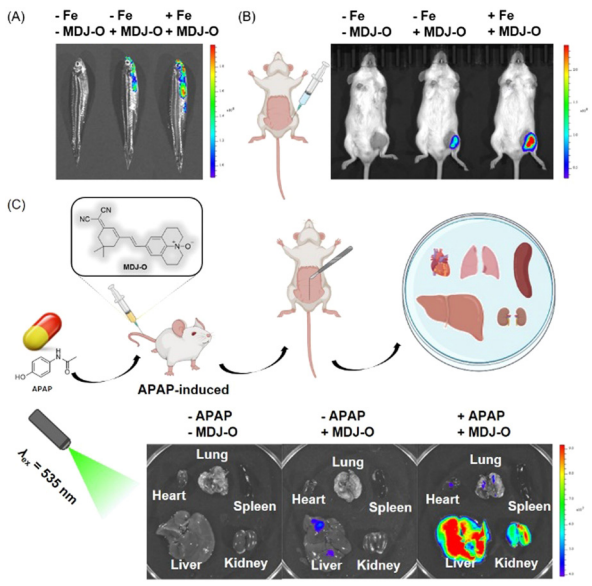

Fig. 5 (A) Fluorescence images of zebrafish: adult zebrafish only, adult zebrafish cultivated with **MDJ-O** (10 μM), adult zebrafish pretreated with Fe^{2+} (100 μM) before incubation with **MDJ-O** (10 μM) ($\lambda_{ex}/\lambda_{em}$ = 535/720 nm). (B) Imaging of Fe^{2+} in living mice with **MDJ-O**. (C) Fluorescence imaging of the main organs of mice ($\lambda_{ex}/\lambda_{em}$ = 535/720 nm).

zebrafish gradually increased, exhibiting a concentration-dependent relationship (Fig. S28, ESI†). The above results illustrated that **MDJ-O** could easily enter the zebrafish and detect Fe^{2+} in the living zebrafish.

As shown in Fig. 5B, the mice had no fluorescence background interference. When **MDJ-O** (100 μM, 100 μL) was injected into the right leg muscle of a living mouse, a certain fluorescence signal was observed just for 5 min in the right leg of the mice under 535 nm light irradiation. This phenomenon suggested that **MDJ-O** could detect endogenous Fe^{2+} in living mice. After *in situ* intramuscular injection of **MDJ-O** (100 μM, 100 μL) followed by $FeSO_4$ (1 mM, 100 μL) to the right leg of mice, the fluorescence signal was significantly enhanced. This phenomenon revealed that probe **MDJ-O** could recognize exogenous Fe^{2+} in mice. In conclusion, **MDJ-O** could realize the visualization of Fe^{2+} in mice and could be used as a valuable NIR fluorescent probe for rapid imaging of endogenous and exogenous Fe^{2+} *in vivo*.

Imaging of Fe^{2+} in APAP-induced liver and kidney injury

Drug-induced liver and kidney injury are the main reason for acute liver and kidney injury, which seriously threaten human health and has attracted extensive attention from many researchers and clinicians. The damage process is often associated with the increased Fe^{2+} level in the internal liver and kidneys. Therefore, monitoring of Fe^{2+} in the liver and kidney tissues is of great significance. Here, a liver and kidney injured mouse model was introduced by tail vein injection of APAP (300 mg kg^{-1}, 300 μL) to the mouse. As displayed in Fig. 5C, the fluorescence intensities of the liver and kidney treated with APAP were significantly enhanced, while the fluorescence of other organs was weak. After sequential injection of Bpy, APAP, and **MDJ-O** *via* the tail vein, the fluorescence intensities of the liver and kidney were decreased (Fig. S29, ESI†). This phenomenon illustrated that the enhancement of the fluorescence intensity was closely related to the increase of the Fe^{2+} level. As displayed in Fig. S30 (ESI†), only the liver treated with **MDJ-O** had weak fluorescence, which might be due to the ethanol solvent that dissolved the probe and damaged the liver. To verify that APAP indeed induced liver and kidney injury in mice, tissue slice scanning experiments were performed (Fig. S30 and S31, ESI†). As shown in Fig. S30 (ESI†), the hematoxylin and eosin (HE) stained liver and kidney sections exhibited significant degeneration, while the liver and kidney sections of normal mice did not show obvious damage. The above results indicated that the liver and kidney were damaged after APAP treatment. According to the literature, there were no studies on the simultaneous monitoring of liver and kidney damage through fluorescence imaging of changes in Fe^{2+}. The above data implied that probe **MDJ-O** had potential to visualize APAP-induced liver and kidney injury. The probe has the potential to become a useful tool for the diagnosis and evaluation of drug-induced liver and kidney injury.

Conclusions

In conclusion, a novel NIR fluorescent probe **MDJ-O** was designed and synthesized. An *N*-oxide structure as the reaction site for Fe^{2+} was introduced to **MDJ-O**. This probe can monitor Fe^{2+} in nearly 100% aqueous systems. When the probe was deoxidized by Fe^{2+}, NIR fluorescence (λ_{em} = 720 nm) was turned on, and the color of the solution changed from colorless to purple, enabling both colorimetric and fluorescence detection of Fe^{2+} by **MDJ-O**. The response mechanism of **MDJ-O** towards Fe^{2+} has been confirmed using absorption spectroscopy, emission spectroscopy, ESI-MS analysis, HPLC study, and DFT calculations. The optical evaluation showed that the detection limit of **MDJ-O** for Fe^{2+} is as low as 3.09×10^{-6} M. In addition, **MDJ-O** has excellent selectivity and a rapid response for Fe^{2+}. This probe can realize the detection of Fe^{2+} in a wide pH range (4–11). Hypotoxic **MDJ-O** has strong penetrability and a high signal-to-noise ratio in cells and *in vivo*. The NIR probe **MDJ-O** has been successfully applied to the fluorescence imaging of Fe^{2+} in living cells, zebrafish, and mice. Notably, **MDJ-O** was utilized to visualize Fe^{2+} in an APAP-induced liver and kidney injury model. This is of great significance for further understanding the mechanism of drug-induced liver and kidney injury. These results indicated that **MDJ-O** has great potential in detecting Fe^{2+}.

Author contributions

Hanyue Xiang: synthesis and characterization of compounds, data curation, formal analysis, validation, and writing – original draft. Yanjie Song: investigation, data curation, and formal analysis. Yilin Wang: investigation, data curation, and formal analysis. Wenzhuo Fu: investigation and resources. Nao Xiao: supervision, project administration, fund acquisition, concept formation, and writing – review and editing.

Conflicts of interest

There are no conflicts to declare.

Acknowledgements

This work was supported by the Scientific Research Cultivating Fund of Capital Medical University, China (PYZ21023) and the Open Fund of the Key Laboratory of Analytical Chemistry for Living Biosystems, Chinese Academy of Sciences, China (ACL202201).

Notes and references

1 J. C. Yang, Q. M. Li, Y. Feng and Y. H. Zeng, *Int. J. Mol. Sci.*, 2023, **24**, 6891.
2 A. D. Read, R. E. T. Bentley, S. L. Archer and K. J. Dunham-Snary, *Redox Biol.*, 2021, **47**, 102164.
3 P. T. Morraja, G. Rique-Pujol, C. Muller-Sanchez, M. Reina, O. M. Martinez-Estrada and F. X. Soriano, *Int. J. Mol. Sci.*, 2023, **24**, 922.
4 X. Chen, C. H. Yu, R. Kang, G. Kroemer and D. L. Tang, *Cell Death Differ.*, 2021, **28**, 1135–1148.

5 D. G. Liang, A. M. Minikes and X. J. Jiang, *Mol. Cell*, 2022, **82**, 2215–2227.
6 X. J. Jiang, B. R. Stockwell and M. Conrad, *Nat. Rev. Mol. Cell Biol.*, 2021, **22**, 266–282.
7 Z. Zhao, *Free Radical Biol. Med.*, 2023, **208**, 510–515.
8 R. Hider, M. V. Aviles, Y. L. Chen and G. O. Latunde-Dada, *Int. J. Mol. Sci.*, 2021, **22**, 1278.
9 Y. Song, M. Ismail, Q. Shan, J. Zhao, Y. Zhu, L. Zhang, Y. Du and L. Ling, *Nanoscale*, 2021, **13**, 20170–20185.
10 Q. Q. Xu, X. L. Cheng, B. Y. Zhang, F. Zhang, X. Wang, S. S. Li and Y. X. Zhang, *Anal. Chim. Acta*, 2022, **1232**, 340472.
11 Q. W. Pan, F. Lin, R. Q. Liu, Y. L. Li, X. Y. Zhang, R. Luo, L. L. Cai, Y. Liu, W. G. Deng and L. R. He, *Chem. Eng. J.*, 2023, **466**, 142962.
12 H. Shi, L. Jin, J. Li, K. Liang, X. Li, Z. Ye, X. Zhu, J. M. Oliveira, R. L. Reis, Z. Mao and M. Wu, *J. Mater. Chem. B*, 2022, **10**, 6351–6359.
13 M. Baruah, A. Jana, M. Ali, K. Mapa and A. Samanta, *J. Mater. Chem. B*, 2022, **10**, 2230–2237.
14 T. Wang, J. Zhang, H. Zhang, W. Bai, J. Dong, Z. Yang, P. Yang, Z. Gu, Y. Li, X. Chen and Y. Xu, *J. Mater. Chem. B*, 2022, **10**, 7875–7883.
15 S. D. Wang, Z. J. Liu, J. F. Geng, L. G. Li and X. J. Feng, *Biomed. Pharmacother.*, 2022, **153**, 113374.
16 X. Chen, R. Kang, G. Kroemer and D. L. Tang, *Nat. Rev. Clin. Oncol.*, 2021, **18**, 280–296.
17 L. Zhao, X. X. Zhou, F. Xie, L. Zhang, H. Y. Yan, J. Huang, C. Zhang, F. F. Zhou, J. Chen and L. Zhang, *Cancer Commun.*, 2022, **42**, 88–116.
18 X. Chen, R. Kang, G. Kroemer and D. L. Tang, *J. Exp. Med.*, 2021, **218**, e20210518.
19 L. X. Li, F. F. Guo, H. Liu and T. Zeng, *Cell. Mol. Life Sci.*, 2022, **79**, 201.
20 J. Y. Chen, X. P. Li, C. D. Ge, J. X. Min and F. D. Wang, *Cell Death Differ.*, 2022, **29**, 467–480.
21 Y. Qin, T. Guo, Z. Wang and Y. Zhao, *J. Mater. Chem. B*, 2021, **9**, 4793–4803.
22 C. Bunchorntavakul and K. R. Reddy, *Clin. Liver Dis.*, 2018, **22**, 325–346.
23 C. Liu, X. Li, M. Gao, Y. Dong and Z. Chen, *JHEP Rep.*, 2023, **5**, 100766.
24 J. Y. Akakpo, A. Ramachandran, H. Orhan, S. C. Curry, B. H. Rumack and H. Jaeschke, *Toxicol. Appl. Pharmacol.*, 2020, **409**, 115317.
25 X. Zeng, J. Chen, S. Yu, Z. Liu and M. Ma, *J. Lumin.*, 2022, **25**, 119069.
26 L. Wu, J. Liu, X. Tian, R. R. Groleau, S. D. Bull, P. Li, B. Tang and T. D. James, *Chem. Sci.*, 2021, **12**, 3921–3928.
27 S. Feng, J. Zheng, J. Zhang, Z. Gui and G. Feng, *Sens. Actuators, B*, 2022, **371**, 132512.
28 L. Wu, Q. Ding, X. Wang, P. Li, N. Fan, Y. Zhou, L. Tong, W. Zhang, W. Zhang and B. Tang, *Anal. Chem.*, 2020, **92**, 1245–1251.
29 R. Troìa, M. Gruarin, C. Grisetti, F. Serafini, L. Magna, E. Monari, M. Giunti and F. Dondi, *J. Vet. Intern. Med.*, 2018, **32**, 1372–1382.
30 F. Y. Liu, X. Y. Zhu, Y. Wang, Q. Y. Yi, C. X. Pu, Y. Luo, J. Y. Wang and M. Wang, *Sens. Actuators, B*, 2023, **374**, 132840.
31 J. J. Yang, M. T. Fan, Y. Sun, M. Y. Zhang, Y. T. Xue, D. Z. Zhang, T. Wang and X. Y. Cui, *Sens. Actuators, B*, 2020, **307**, 127652.
32 Y. Y. Liu, S. Naha, N. Thirumalaivasan, S. Velmathi and S. P. Wu, *Sens. Actuators, B*, 2018, **277**, 673–678.
33 Y. Hu, L. M. Lu, S. M. Guo, X. L. Wu, J. Y. Zhang, C. S. Zhou, H. Y. Fu and Y. B. She, *Sens. Actuators, B*, 2023, **382**, 133534.
34 Q. Chen, X. F. Zhang, T. Wang, X. Q. Cao and S. L. Shen, *Anal. Chim. Acta*, 2022, **1231**, 340443.
35 X. Z. Wei, T. Zhu, Y. S. Ma, J. Y. Sun, G. X. Zheng, T. B. Ma, X. F. Yang, Z. L. Song, Y. F. Lv and J. Zhang, *Sens. Actuators, B*, 2023, **380**, 133392.
36 Q. Lin, C. S. Li, L. J. Wang, H. M. Cai, L. P. Tang and Y. Q. Gu, *Sens. Actuators, B*, 2022, **371**, 32521.
37 L. N. Guo, X. C. Chen, R. J. Xie, L. M. Han and N. Zhu, *J. Mol. Struct.*, 2023, **1275**, 134615.
38 M. Das, V. K. Madduluri, V. Jaswal and M. Sarkar, *J. Photochem. Photobiol., A*, 2022, **429**, 113896.
39 R. Kakiuchi, T. Hirayama, D. Yanagisawa, I. Tooyama and H. Nagasawa, *Org. Biomol. Chem.*, 2020, **18**, 5843–5849.
40 C. H. Cai, H. L. Wang and R. J. Man, *Spectrochim. Acta, Part A*, 2021, **255**, 119729.
41 T. Hirayama, K. Okuda and H. Nagasawa, *Chem. Sci.*, 2013, **4**, 1250.
42 R. Roy, A. Khan, T. Dutta and A. L. Koner, *J. Mater. Chem. B*, 2022, **10**, 5352–5363.
43 L. Kong, W. Lu, X. Cao, Y. Wei, J. Sun and Y. Wang, *J. Mater. Chem. B*, 2022, **10**, 7924–7954.
44 C. Shao, Y. Liu, Z. Chen, H. Zhu, J. Zhao and Y. Qian, *Cell Chem. Biol.*, 2022, **29**, 43–56.
45 T. Qian, X. Zhao, T. Jia, S. Si, Z. Xu, B. Liu, H. Xu and C. Zhao, *Spectrochim. Acta, Part A*, 2022, **280**, 121517.
46 H. Zhou, J. Tang, L. Sun, J. Zhang, B. Chen, J. Kan, W. Zhang, J. Zhang and J. Zhou, *Sens. Actuators, B*, 2019, **278**, 64–72.
47 A. V. Marenich, C. J. Cramer and D. G. Truhlar, *J. Phys. Chem. B*, 2009, **113**, 6378–6396.
48 S. Grimme, J. Antony, S. Ehrlich and H. Krieg, *J. Chem. Phys.*, 2010, **132**, 154104.
49 M. P. Almeida, J. M. Welker, S. Siddiqui, J. Luiken, S. C. Ekker, S. C. Ekker, K. J. Clark, J. J. Essner and M. McGrail, *Nature*, 2021, **11**, 1732.
50 S. Feng, J. Zheng, J. Zhang, Z. Gui and G. Feng, *Sens. Actuators, B*, 2022, **371**, 132512.